Journal Name

ARTICLE TYPE

Cite this: DOI: 00.0000/xxxxxxxxxx

Revealing the complex structure of molten FLiBe ($2LiF-BeF_2$) by experimental X-ray scattering, neutron scattering, and deep neural network-based molecular dynamics

Sean Fayfar,[a] Rajni Chahal,[b] Haley Williams,[c] D. Nathanael Gardner,[c] Guiqiu Zheng,[a] David Sprouster,[ad] Jörg C. Neuefeind,[e] Dan Olds,[f] Andrea Hwang,[g] Joanna Mcfarlane,[h] Ryan C. Gallagher,[h] Mark Asta,[g] Stephen Lam,*[b] Raluca O. Scarlat,*[c] and Boris Khaykovich*[a]

Received Date
Accepted Date

DOI: 00.0000/xxxxxxxxxx

The use of molten salts as coolants, fuels, and tritium breeding blankets in the next generation of fission and fusion nuclear reactors benefits from furthering the characterization of the molecular structure of molten halide salts, paving the way to predictive capability of chemical and thermo-physical properties of molten salts. Due to its neutronic, chemical, and thermo-chemical properties, $2LiF-BeF_2$ is a candidate molten salt for several fusion and fission reactor designs. We perform neutron and X-ray total scattering measurements to determine the atomic structure of $2LiF-BeF_2$. We also perform ab-initio and neural network molecular dynamics simulations to predict the structure obtained by neutron and X-ray diffraction experiments. The use of machine learning provides improvements to the efficiency in predicting the structure at a longer length scales than is achievable with ab-initio simulations at significantly lower computational expense while retaining near ab-initio accuracy. The comparison among experimental and modeling results at a higher resolution and efficiency than previous measurements provides the opportunity to explore the structural determination of $2LiF-BeF_2$ beyond the first-nearest neighbor analysis that had been previously achieved with X-ray diffraction measurements of a FLiBe melt. This work may serve as a reference for future studies of salt structure and macroscopic properties with and without the addition of solutes.

1 Introduction

Molten salts have garnered a resurgence of interest due to their favorable use in energy applications such as advanced next-generation nuclear power plants.[1–3] These include fluid-fueled molten salt reactors (MSRs) which employ fluoride or chloride salts,[4,5] solid-fueled reactors which employ salt as a high-temperature coolant such as the fluoride-salt-cooled high temperature reactor (FHR),[6] and fusion reactors such as the affordable, robust, compact (ARC) reactor which uses $2LiF-BeF_2$ as both a coolant and a tritium breeding blanket.[7,8] Molten salts provide high volumetric heat capacity and a wide range of thermal stability that allow reactors to deliver a larger fraction of their heat at higher temperatures compared with traditional designs. This increase in heat-to-electricity efficiency, along with the possibility of diverse energy products at higher temperatures, enhances the economic competitiveness of salt-based nuclear energy systems.[9,10] Additionally, the ability to operate at nearly atmospheric pressure enables design of passive safety systems and inherent safety features which help meet high safety standards with greater simplicity of design and, consequently, with potentially lower development costs and shorter development timelines.[11,12]

A number of salt compositions are candidates for use in MSRs with $2LiF-BeF_2$ (FLiBe) being the focus of this study.[13–17] Experimentally determining the thermo-physical properties such as

[a] Nuclear Reactor Laboratory, Massachusetts Institute of Technology, Cambridge, MA 02139, USA; E-mail: bkh@mit.edu
[b] Department of Chemical Engineering, University of Massachusetts Lowell, Lowell, Massachusetts 01854, United States; E-mail: Stephen_Lam@uml.edu
[c] Department of Nuclear Engineering, University of California, Berkeley, CA 94720, USA; E-mail: scarlat@berkeley.edu
[d] Department of Materials Science and Chemical Engineering, Stony Brook University, Stony Brook, NY, 11784, USA
[e] Neutron Sciences Directorate, Oak Ridge National Laboratory, Oak Ridge, Tennessee 37831-6475, United States
[f] National Synchrotron Light Source II, Brookhaven National Laboratory, Upton, NY, 11973, USA
[g] Department of Materials Science and Engineering, University of California, Berkeley, CA 94720 USA
[h] Fusion and Fission Energy and Science Directorate, Oak Ridge National Laboratory, Oak Ridge, Tennessee 37831-6475, United States

† Electronic Supplementary Information (ESI) available: [details of any supplementary information available should be included here]. See DOI: 00.0000/00000000.

the density, viscosity, thermal expansion, specific heat, and others has been the focus of a number of studies.[18–26] Electroanalytical studies have sought to characterize ionic transport as well as the liquidus in $LiF-BeF_2$ systems.[27?,28] Additional studies have focused on measuring the atomic structure of molten salt candidates[29–32] and their corrosive effects on structural materials.[33–38] With the vast possibilities of salt compositions, predictive modeling can alleviate experimental bottlenecks associated with characterizing new salt mixtures.[39–41] To successfully ascertain the physical characteristics of molten salts using simulations, their atomic structure needs to be measured experimentally to validate the assumptions required in simulations.

The structure of molten $LiF-BeF_2$ solutions was studied by X-ray diffraction fifty years ago by Vaslow and Narten[42] using a MoK_α lab X-ray source. They verified tetrahedral geometry for BeF_4^{2-} complex ions as in the model developed by Baes[43], and output first nearest-neighbor (FNN) distances and coordination numbers (CN) for Be−F, Li−F, and F−F. They postulated corner sharing tetrahedra, showing a consistent Be−F CN of 4 for binary melts across the entire composition space from 100% LiF to 100% BeF_2. This postulation was further supported by molecular dynamics models that predict FNN and CN for $LiBeF_3$; the Be−F values were within two standard deviations, F−F were identical between molecular dynamic (MD) predictions and experiments, and Li−F FNN distance predicted by MD at 760 °C was more than three standard deviations smaller than X-ray-measured values at 400 °C.[44]

Evidence of tetrahedral BeF_4^{2-} in molten $LiF-BeF_2$ solutions is ubiquitous, beginning with measurements using X-ray diffraction and vibrational spectroscopy (infrared and Raman) along with molecular dynamics studies.[42,44–46] Evidence of dimers and higher order oligomers increasing with the BeF_2 concentration has followed from Raman spectroscopy and thermodynamic models fit to measured activity coefficients and other thermo-chemical data.[41,47–49] The formation of corner-sharing tetrahedral BeF_4^{2-} clusters (which was proposed from considering fluoroberyllate melts as analagous to SiO_4 melts)[43] has been reinforced by modern molecular dynamics simulations.[39,41,50–52] However, the ability to validate the intermediate-range melt structure predicted in molecular simulations is limited by the resolution of experimental X-ray diffraction data available in the literature.[42] With the FNN structure of fluoro-beryllate melts described and validated, it now becomes possible to investigate the role of intermediate-range order on solvation mechanisms and other macroscopic physical and chemical properties of fluids. Thus, validating molecular dynamics models for their structure predictions beyond FNN would be highly impactful.

Molecular dynamics simulations have revolutionized the ability of researchers to discover and assess new materials, aiding interpretation, error analysis, sensitivity analysis and prioritization of experimental studies. Ab-initio molecular dynamics simulations (AIMD) have been the premier method for modeling molten salt structure and predicting physical properties.[40] However, due to high computational costs, AIMD simulations are practically limited to small system sizes (less than hundreds of atoms). Meanwhile, classical interatomic potentials can simulate large system sizes, but have recently been shown to inaccurately predict relative populations of bond angles and clusters, which play an important role in determining the thermo-physical and thermo-chemical behavior in structurally-complex salt mixtures.[53] While such simulations have been used to interpret the general features and structures that exist in an experimental X-ray or Raman spectra, precise reconstruction and detailed analysis has not been possible. To overcome these limitations, recent developments of neural network molecular dynamics simulations (NNMD) have demonstrated that NNMD simulations can achieve near ab-initio accuracy, at orders of magnitude higher speed and scalability, for predicting the structures and properties of molten salts.[54–58] Moreover, it was recently shown that larger NNMD simulations were required for accurately capturing the intermediate-range structures beyond the first solvation shell that can emerge in salts containing significant fraction of multivalent cations such as Zr.[53] Structures of similar length scale have also been predicted for $LiF-BeF_2$ with dissolved tritium.[59,60]

In this work, we present a structural characterization of molten FLiBe including total scattering measurements and molecular dynamics simulations. We examined FLiBe using both neutron and X-ray diffraction from room temperature up to 700 °C, well above the melting point. Our measurements, conducted using renowned sychrotron X-ray and spallation neutron facilities, enabled higher resolution than prior X-ray diffraction measurements and a degree of detail inaccessible to previous studies. These high-resolution measurements are necessary to validate new molecular dynamics techniques. We performed AIMD and NNMD simulations to interpret the structural peaks found in measurements, and we provide several validation experimental datasets for both short-range and intermediate-range order in FLiBe melts at multiple temperatures.

2 Experimental and computational methods

2.1 Molecular-dynamics simulations

2.1.1 Ab-initio molecular dynamics simulations

A supercell containing 91 atoms was used (13 Be, 26 Li, and 52 F). The simulation cell volume was imposed based on the FLiBe density of 2.0314 g/mL and 1.937 g/mL at 510 °C and 700 °C, respectively.[61] Assuming natural isotopics for ^{7}Li of 92.5% and 6.94 g/mol Li atomic weight, the cell lengths are 10.17 Å and 10.33 Å, respectively. Recent experiments found the density of FLiBe to be 2.029(11) g/mL and 1.948(14) g/mL at 510 °C and 700 °C, respectively, with a molecular weight of 33.02(5) g/mol, LiF/BeF_2 molar ratio of 1.977, and 93.12% ^{7}Li enrichment.[23] The supercell was first initialized with a random structure generated with the Packmol package to avoid overlapping atomic positions.[62] The initial random configuration was equilibrated at 510 °C and 700 °C for 20 ps to develop the liquid structure. Once equilibrated, nearly 50 ps simulation trajectory should be sufficent to obtain converged molten-salt structure and properties according to our previous work.[63] A time step of 2 fs was used for all AIMD simulations. The pressure of the equilibrated fixed-volume cells was -500 and -300 MPa, respectively (95% confidence interval).

2.1.2 NNIP Training

For training of the neural network interatomic potential (NNIP), DeePMD-kit (DP-kit) package (version 1.3.3) was employed.[64] The Deep-Pot-Smooth Edition (DeepPot-SE) potential contained inside the DP-kit was chosen due to a smooth and continuously differentiable potential energy surface generation.[65] The DeepPot-SE model learns a mapping between local environment of each atom within 8 Å cut-off to a per-atom energy, such that the sum of atomic energies corresponds to reference DFT energy. The gradients of the NNIP predicted energies are then used to compute the atomic forces. Both the reference energies and forces are included to evaluate the loss function which is minimized during training of a DeepPot-SE model. The training dataset comprised 11019 configurations at 510 °C and 10283 configurations at 700 °C containing LiF and BeF_2 of AIMD simulations with 91 atom supercells. During the training, the datasets were shuffled and were split in 80% and 20% for training and validation, respectively. Here, the smooth cutoff and hard cutoff radius of 2 Å and 8 Å were chosen. The embedding network and fitting network size were {25,50,100} and {240,240,240}, respectively. The tunable prefactors in loss function were chosen at 0.002, 1000, 1, and 1 for p_e^{start}, p_f^{start}, p_e^{limit}, and p_f^{limit}, respectively. These network parameters previously resulted in well-fitted potential energy surface for multicomponent molten salt systems.[53,56] Here, the network was only trained on AIMD energies and forces. The trained network using DeepPot-SE yielded energy and force errors of 1.92 meV/atom and 22.1 meV/Å, respectively. The resulting errors are within the precision of DFT. The low energy and force training testing errors suggest a well-fitted potential energy surface.

2.1.3 Neural network molecular dynamics using developed NNIP

The trained NNIP potentials were used in Large Scale Atomic/Molecular Massively Parallel Simulator (LAMMPS) via the interface with DeePMD-kit.[66] The NNIP-based molecular dynamics (NNMD) simulations allow for simulating larger simulation cell parameters that are required to gain sufficient resolution at $Q \sim 1\,\text{Å}^{-1}$. For this purpose, the cell parameters of 20.33 Å and 20.66 Å were chosen for NNMD simulations of FLiBe at 510 °C and 700 °C, respectively, comprising 728 atoms (208 Li, 104 Be, 416 F), and corresponding to liquid densities of 2.0314 g/mL and 1.937 g/mL, respectively. During NNMD simulations, at least 2 ns simulations were performed using 2 fs time steps employing Nosé-Hoover thermostat[67] in constant volume ensemble (NVT). Periodic boundary conditions were maintained in all three directions. After 0.5 ns of equilibration, trajectories longer than 1.5 ns were used to study radial distribution functions as well as to perform structure factor calculations. More details on the analysis are provided in the following sections.

2.2 Sample preparation

A 2:1 stoichiometric ratio of LiF and BeF_2 was prepared with isotopically enriched lithium-7 fluoride provided by Oak Ridge National Laboratory (ORNL) and beryllium fluoride from Materion. To prepare the sample for neutron scattering measurements, a 1.3(1) g sample of FLiBe was placed and melted in a vanadium canister and sealed with a flanged titanium lid and a graphite foil gasket. The sample was subsequently cleaned from beryllium contamination (below the free release limit of $0.2\,\mu g/100cm^2$). For X-ray scattering measurements, a sample of FLiBe (prepared from constituent Materion salts) was loaded and melted into a capped graphite insert then placed into a flame sealed quartz NMR tube.[32]

The ^{7}Li enriched sample used in this study was believed to be approximately 99% enrichment, though the stock ^{7}LiF was a legacy sample from ORNL and was not labeled with a numerical value. Readily available enriched Li from Sigma-Aldrich is available at 99%. We include a comparison between a 99% and 95% ^{7}Li enriched sample in Fig. S4† by weighting the NNMD results.

2.3 Neutron and X-ray scattering

Neutron total scattering measurements were performed at the NOMAD beamline[68] at the Spallation Neutron Source (SNS). Samples were loaded into vanadium sample cans and placed into the vanadium furnace to measure the sample from room temperature up to 700 °C. The sample was heated using the vanadium furnace provided at the beamline; the sample was measured upon heating with an exposure time of 5 minutes for each measurement. Once the sample reached 550 °C and 700 °C, the sample was measured for 7.6 hours at each temperature. The measurements at the beamline were calibrated using standard samples such as diamond and vanadium. The measurements were background corrected by subtracting the empty sample container.[68] The raw neutron scattering intensity was converted to the total (static) structure factor $S(Q)$ with corrections using the software ADDIE[69] at the beamline (shown in Figs. S5† and S6†). Q is the scattering vector and is defined as $Q = \frac{4\pi}{\lambda}\sin\theta$ for elastic scattering, where λ is the wavelength of the radiation and 2θ is the diffraction angle.

X-ray diffraction measurements were conducted at the PDF beamline (28-ID-1)[70] at the National Synchrotron Light Source II (NSLS-II). The sample was placed in a novel sample holder designed to contain molten salts that includes a sealed quartz capillary with a capped graphite insert to hold the salt.[32] The X-ray measurements were performed with an amorphous silicon-based flat panel detector mounted orthogonal to the beam path that moved between two distances for pair distribution function (PDF) and X-ray diffraction (XRD) measurements.[70] The distance was calibrated by measuring a LaB_6 standard sample. The sample was heated using a hot-air blower at a rate of 5 °C per minute until reaching 510 °C. The sample was measured while heating with an exposure time of 30 seconds for each measurement. Once at 510 °C, the sample was measured with an exposure time of approximately 5 minutes. The raw 2D detector images were corrected using standard procedures such as subtracting the detector dark current and masking regions with artifacts. The corrected images were radially integrated and converted into the scattering intensity as a function of the scattering vector Q.[71] Patterns were also measured of the empty graphite quartz container and

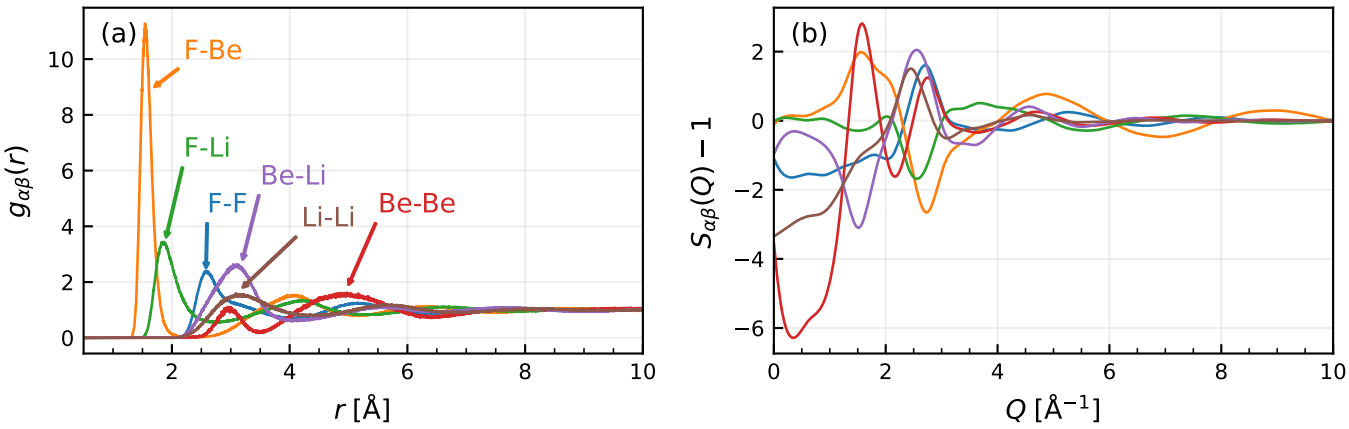

Fig. 1 NNMD simulation results of the (a) unweighted partial PDFs and (b) unweighted partial structure factors of FLiBe at 700 °C

were subtracted from the sample measurements (see Figs S7† and S8†). The X-ray scattering intensities were converted into the total structure factor $S(Q)$ using the software PDFgetX3[72] that uses an *ad hoc* data correction method to obtain the coherent X-ray scattering intensities. The sample temperature was calculated by the methods described in Sprouster *et al.*[32].

The total structure factor $S(Q)$ calculated from the total scattering intensity is composed of partial structure factors dependent on the salt components through

$$S^{(\mathrm{n/x})}(Q) = \sum_{\alpha,\beta\geq\alpha} S^{(\mathrm{n/x})}_{\alpha\beta}(Q) = \sum_{\alpha,\beta\geq\alpha} w^{(\mathrm{n/x})}_{\alpha\beta}(Q) S_{\alpha\beta}(Q) \quad (1)$$

with

$$w^{(\mathrm{n/x})}_{\alpha\beta}(Q) = \frac{c_\alpha c_\beta f_\alpha(Q) f_\beta(Q)}{\left[\sum_\alpha c_\alpha f_\alpha(Q)\right]^2}\left(2-\delta_{\alpha\beta}\right), \quad (2)$$

where α and β are coefficients representing the salt components, c is the concentration of the atomic species, $f(Q)$ is the X-ray form factor,[73] and $\delta_{\alpha\beta}$ is the Kronecker delta function. The weights $w_{\alpha\beta}$ are normalized such that they sum to one for all values of Q. For neutron scattering, the X-ray atomic form factors are replaced with the neutron scattering lengths b that are independent of Q. The superscripts indicate that the structure factor or PDF was weighted using Eq. (2) for neutrons (n) or X-rays (x). A discrete Fourier sine transform is used to calculate the pair distribution function (PDF) $g(r)$ as

$$g(r) - 1 = \frac{1}{2\pi^2\rho_0}\sum_{Q}^{Q_{\max}} Q\left[S(Q)-1\right]\frac{\sin Qr}{r}\Delta Q, \quad (3)$$

where ρ_0 is the average number density and r is the distance from a reference atom. The inverse Fourier sine transform calculates the structure factor from the PDF:

$$S(Q) - 1 = 4\pi\rho_0 \sum_{r}^{r_{\max}} r\left[g(r)-1\right]\frac{\sin Qr}{Q}\Delta r. \quad (4)$$

The PDF is the ratio of the atomic density a distance r from a central atom to the bulk density.[74–77] Note, the unweighted partial PDF $g_{\alpha\beta}$ that we discuss is also commonly referred to as the radial distribution function (RDF).[39,52,56,60]

2.4 Coordination numbers calculations

The coordination numbers (CN), $N(r)$, were calculated by integrating the area under the partial PDF using

$$N(r_{\min}) = 4\pi\rho_\beta\int_0^{r_{\min}} r^2 g_{\alpha\beta}(r)dr = \frac{4\pi\rho_\beta}{w^{(\mathrm{n/x})}_{\alpha\beta}}\int_0^{r_{\min}} r^2 g^{(\mathrm{n/x})}_{\alpha\beta}(r)dr, \quad (5)$$

where $\rho_\beta = c_\beta\rho_0$ is the number density of the β-atoms around a central α-atom.[39,76,78] The $r_{\min}$ value is chosen as the first minimum in the partial PDFs.

The first peak locations were determined by fitting the simulated partial PDFs with a skewed Gaussian and calculating the location of the maximum. The error estimate comes from the fitting procedure. To find the first peak locations for the neutron and X-ray measurements, we fitted our results with three skewed Gaussians summed together. The peak location was calculated by finding the maximum point on the component Gaussians. The experimental coordination numbers were calculated by integrating the component Gaussian and removing the weight factor as shown in Eq. (5).[79–81] We performed this same procedure on the neutron weighted NNMD $g^{\mathrm{n}}(r)$ to gauge the accuracy of recovering the partial PDFs from the experimental measurements (see Figs. S10† and S11†). We confirmed that the peak position was retrievable, and we used the comparison to estimate the uncertainty. Calculating the coordination number was only feasible with the Be−F peak because it had a clear minimum at zero and did not overlap with too many other partials. Integrating the fitted Gaussian to the NNMD $g^{\mathrm{n}}(r)$ at 700 °C calculates the CN to be 3.82 as compared to 3.97 from directly integrating $g_{\alpha\beta}(r)$. Using these methods on the 510 °C simulations, we find the CN to be 4.07 compared to 4.00. Similar differences were found using the AIMD results. Using the discrepancies in these values, we estimate the uncertainty in the CN to be ±0.15. The X-ray coordination numbers were not feasible using this method because the weight factor $w_{\alpha\beta}$ depends on Q.

We note also that the coordination numbers depend on the cho-

Table 1 Experimental and computational results of the first peak locations and coordination numbers of FLiBe. CNs from AIMD and NNMD are calculated by integrating the partial $g_{\alpha\beta}(r)$ using Eq. (5). *Because neutron diffraction measurements only provide total $g^{n}(r)$, the CNs are determined by integrating Gaussians fit to the total $g^{n}(r)$; we observe the uncertainty introduced by this method to be ±0.15.

	Temp.	First nearest neighbor peak (Å)				r_{min}	CN		
Pair	(°C)	AIMD	NNMD	Neutron	X-ray	(Å)	AIMD	NNMD	Neutron
F−Be	700	1.548(1)	1.546(1)	1.53(1)	-	2.35	3.99(5)	3.97(5)	3.67(15)*
	550	-	-	1.53(1)	-		-	-	3.73(15)*
	510	1.552(1)	1.551(1)	-	1.51(1)		4.00(5)	4.00(5)	-
F−Li	700	1.850(2)	1.849(3)	1.95(2)	-	2.75	4.52(8)	4.50(8)	-
	550	-	-	1.92(2)	-		-	-	-
	510	1.854(2)	1.860(2)	-	1.92(2)		4.63(8)	4.66(8)	-
F−F	700	2.585(5)	2.587(6)	2.53(1)	-		-	-	-
	550	-	-	2.52(1)	-		-	-	-
	510	2.576(4)	2.579(5)	-	2.47(1)		-	-	-

sen cutoff value, r_{min}, at the first minimum $g_{\alpha\beta}(r)$, as shown in Eq. (5). The Be−F partial PDF has a clear minimum at zero, and we use a r_{min} value of 2.35 Å. However, Winner *et al.* [52] argued that r_{min} (referred to as the first-coordination shell radius) for F−Be should be 1.92 Å, which resulted in their CN result of 3.9. Using a r_{min} value of 1.92 Å with our NNMD partials at 700 °C, we find the CN to be 3.89 matching their results more closely.

2.5 Quantifying agreement between experiments and simulations

To evaluate the agreement between simulations and experimental results, we calculated the R_χ factor proposed by Wright [82] and used by others [83–86] which is defined by

$$R_\chi = \left(\sum_i \left[f_{exp}(x_i) - f_{sim}(x_i) \right]^2 / \sum_i f_{exp}^2(x_i) \right)^{1/2}. \quad (6)$$

Here f_{exp} and f_{sim} correspond to measured and simulated $S(Q)$ and $g(r)$, respectively. All of the R-factors are calculated and listed in Table S1†. We evaluated the structure factor from $1 \le Q \le 15$ Å^{-1}, and the PDF from $1 \le r \le 10$ Å, except for the AIMD results which extend to only ∼5 Å.

3 Results

The partial PDFs and partial structure factors predicted by NNMD simulations at 700 °C are shown in Fig. 1 for each of the atomic pairs in FLiBe; the same results from our AIMD simulations, and from prior studies by Winner *et al.* [52] and Attarian *et al.* [51] are provided in Figs. S2† and S3†, all showing similar features. The results of the total structure factor measurements using neutrons and X-rays while heating above and below the melting point of FLiBe are displayed in Fig. 2. At the lower temperatures, the crystalline Bragg beaks are clearly visible until the melting point around 470 °C is reached. At temperatures above the melting point, a few peaks remain, broader and of lower intensity than

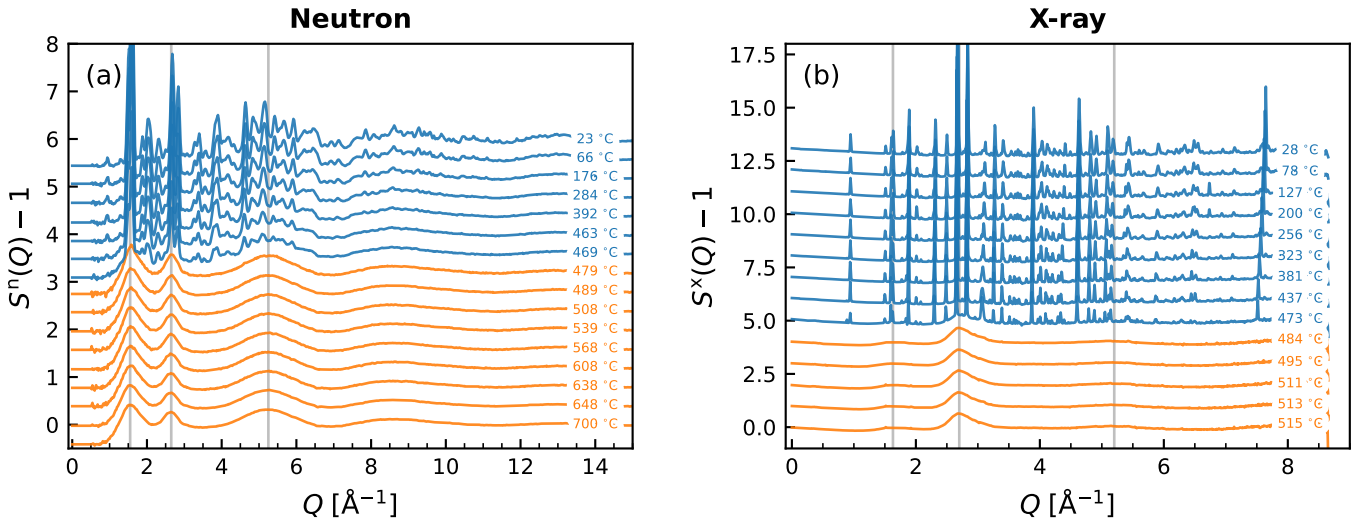

Fig. 2 The total neutron and X-ray structure factor of FLiBe at various temperatures above (orange) and below (blue) the melting point.

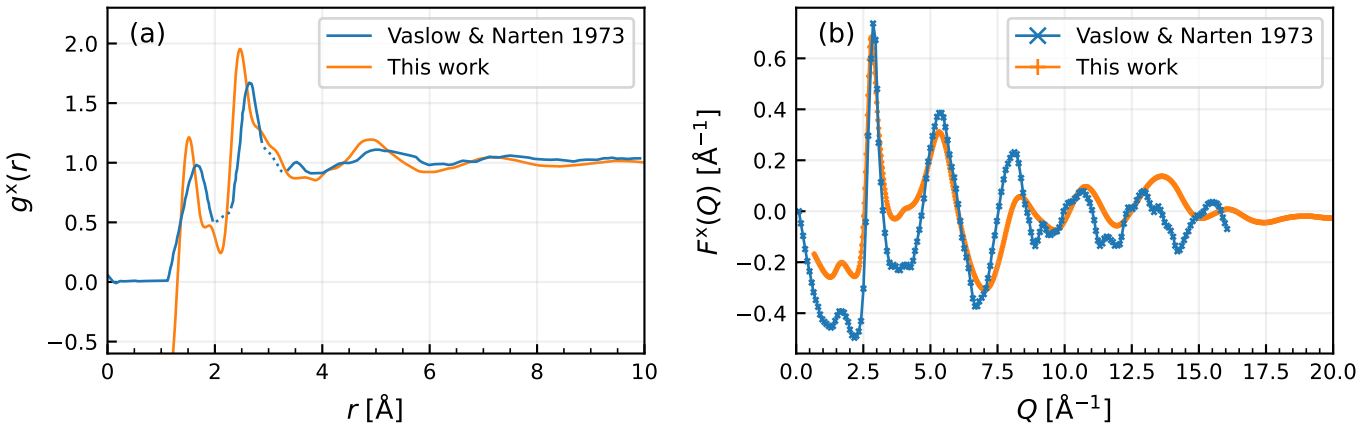

Fig. 3 X-ray PDF and reduced structure function from this study (at 510 °C) and from Vaslow and Narten [42] (at 555 °C). Note, the reduced structure function is defined as $F(Q) = Q[S(Q) - 1]$. The dashed portions of the Vaslow PDF results were reported as artifacts resulting from the limited Q range.

for the solid phase, and most of the higher-Q peaks are no longer present. Once molten, the liquid peaks only have small changes upon further heating with the peak intensity decreasing and moving towards smaller Q values (see Fig. S12[†]).

Our X-ray scattering measurements of molten FLiBe are compared to those measured by Vaslow and Narten [42] and displayed in Fig. 3. We find the small first peak in the reduced structure factor at 1.7 Å^{-1} that Vaslow and Narten [42] observed to increase with the concentration of BeF_2 in LiF−BeF_2 mixtures. The first three peaks in the reduced structure factor match closely in position but vary slightly in intensity likely due to changes in data processing. Our measurements have much higher resolution and extend out further in Q which improves the quality of real space PDF measurements. Our PDF measurements contain the same two large peaks at 1.5 Å and 2.5 Å with slight difference in position and intensity. Additionally, we resolve the small peak at 1.9 Å that was displayed with dashed lines and attributed as artifacts from their limited Q-range.

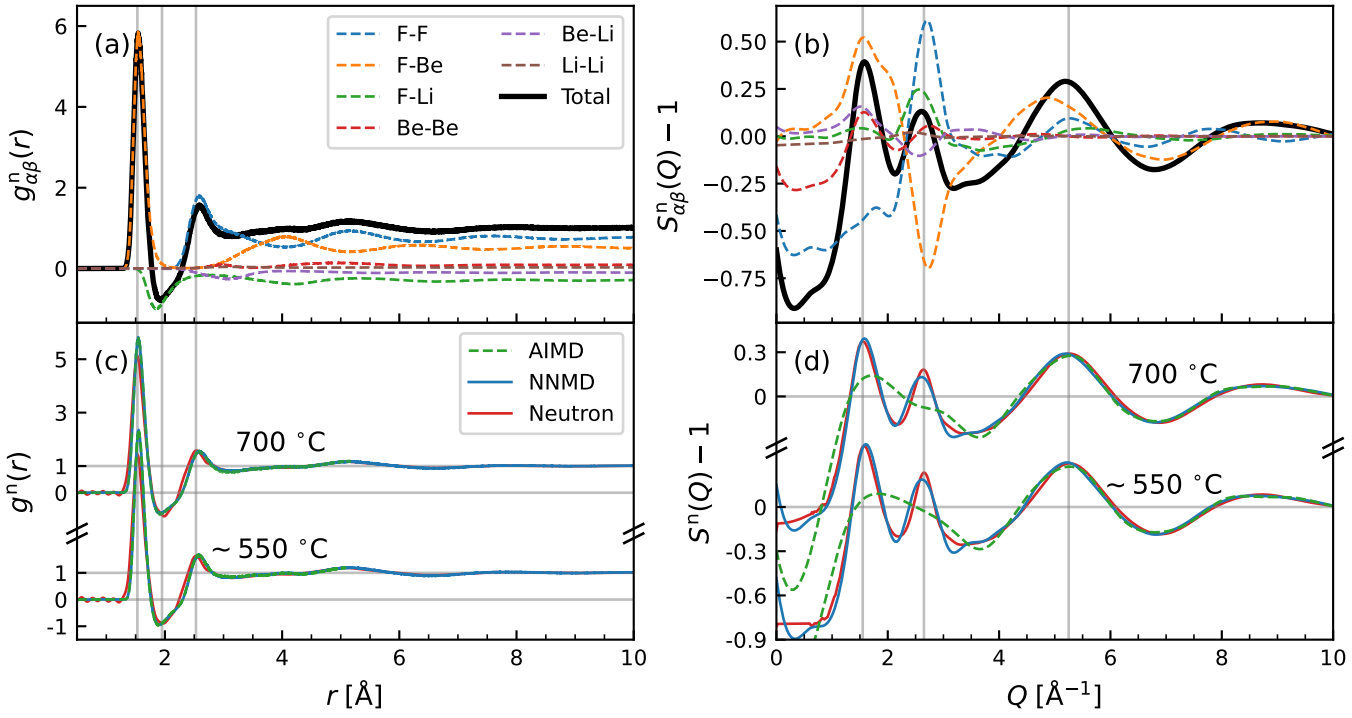

Fig. 4 Experimental and computational results of the neutron PDF and structure factor of FLiBe at 550 °C and 700 °C. (a and b) NNMD simulation results weighted with neutron scattering lengths, and (c and d) neutron scattering results with AIMD and NNMD simulation results for comparison. Note, MD results are at 510 °C.

The results of the total structure factor of FLiBe at 550 °C and 700 °C from neutron measurements are included in Fig. 4, compared with corresponding results from AIMD and NNMD simulations. Using the Fourier transform in Eq. (3), the measured structure factor is used to calculate the PDF in real space. The partial structure factor results from NNMD simulations shown in Fig. 1 were weighted using Eq. (2) and the corresponding neutron scattering lengths to produce the total $g^{\mathrm{n}}(r)$ and $S^{\mathrm{n}}(Q)$ and directly compare with experiments.

These partial PDFs reveal the atomic pairs that produce the peaks measured with experiments such as the main peak at 1.56 Å being the result of Be−F correlations. The first nearest-neighbor peak locations and coordination numbers (CN) are included in Table 1. The neutron and X-ray experimental nearest-neighbor distances in Table 1 are smaller than those found through simulations except for Li−F, and the experimental PDF results are at smaller distances compared with the simulated results.

The results of the structure factor from X-ray diffraction measurements are presented in Fig. 5 with the same AIMD and NNMD simulation results weighted using X-ray atomic form factors. These partial $S^{\mathrm{x}}_{\alpha\beta}$ reveal the atomic correlations producing the scattering peaks such as the first peak at 1.7 $\mathrm{Å}^{-1}$ being comprised of Be−F and F−F that Vaslow and Narten [42] found to increase with BeF_2 concentration. The first peak measured with X-rays around 1.7 $\mathrm{Å}^{-1}$ is significantly weaker than the neutron scattering measurements because the atomic form factor for fluorine is 5 times larger than the other two atoms in FLiBe. This causes a much lower peak than measured with neutrons and is evident with the NNMD X-ray weighted results in Fig. 5b. From the same reasoning, the second peak at 2.7 $\mathrm{Å}^{-1}$ is dominant in the X-ray measurements. The peak position and intensity in the simulated structure factors match closely with the experimental results (Fig. 5d). The small first peak matches better in position and intensity between NNMD simulations and X-ray scattering measurements than the second peak, which is predicted from NNMD simulations to be at slightly lower Q value and weaker intensity than was measured; the peaks at larger Q also follow this trend. The neutron results show this same shift relatively to predicted structure factor, but the difference is less pronounced. To compare all our data, we display neutron and X-ray, NNMD and AIMD partial and total $g(r)$ and $S(Q)$ all vertically aligned in Fig. S1[†].

The partial structure factors in Figs. 4b and 5b help identify the contribution to the first $S(Q)$ peak as having Be−F, Be−Li, and Be−Be components. Using the partial structure factor results from simulations, we can evaluate the charge alternation peaks described by Sharma *et al.* [88] The second peak at 2.7 $\mathrm{Å}^{-1}$ appears to contain the charge alternations that are predicted to have positive correlations with matching cation-cation and anion-anion pairs and negative correlations with opposite pairs. This peak is composed of positive F−F and Be−Be correlations along with negative F−Be correlations. Note that the negative ^{7}Li scattering length causes the F−Li and Be−Li correlation to be opposite of the expected sign in the neutron structure factor.

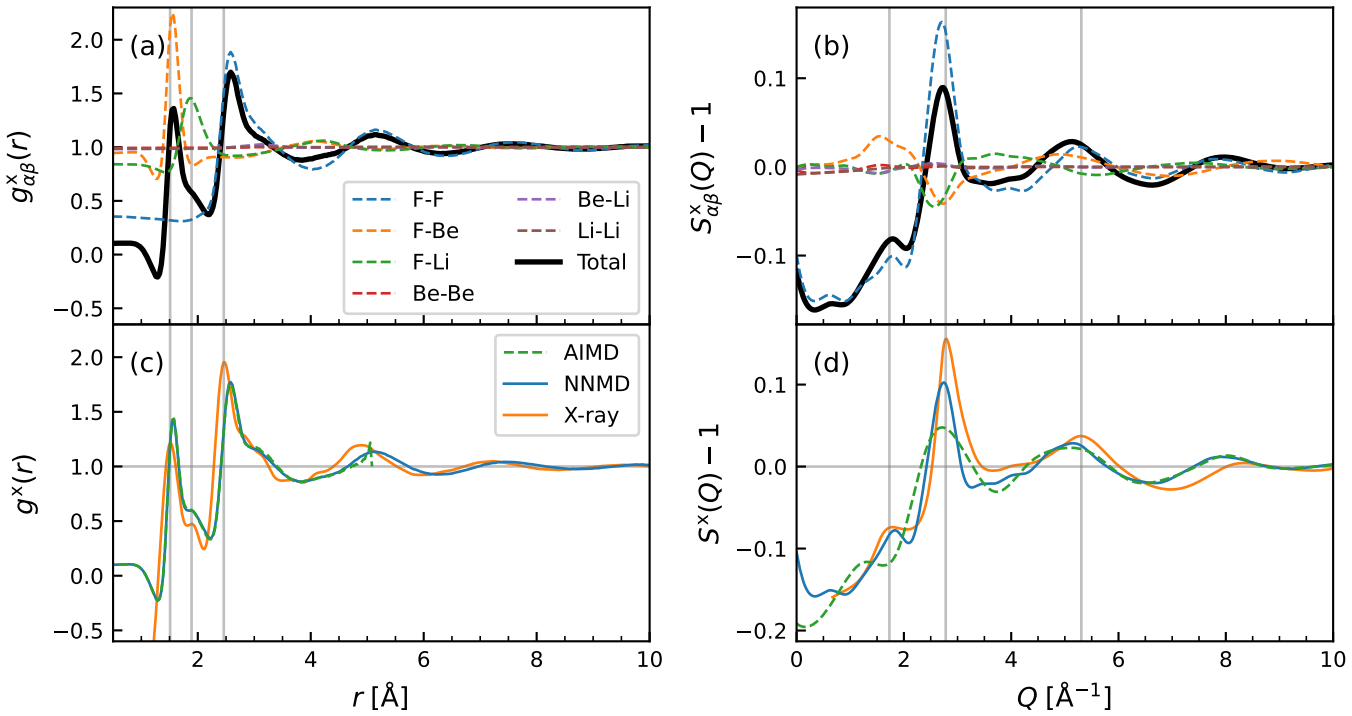

Fig. 5 Experimental and computational results of the X-ray scattering PDF and structure factor of FLiBe at 510 °C. (a and b) NNMD simulation results weighted with the atomic form factors, and (c and d) X-ray scattering results with AIMD and NNMD simulation results for comparison.

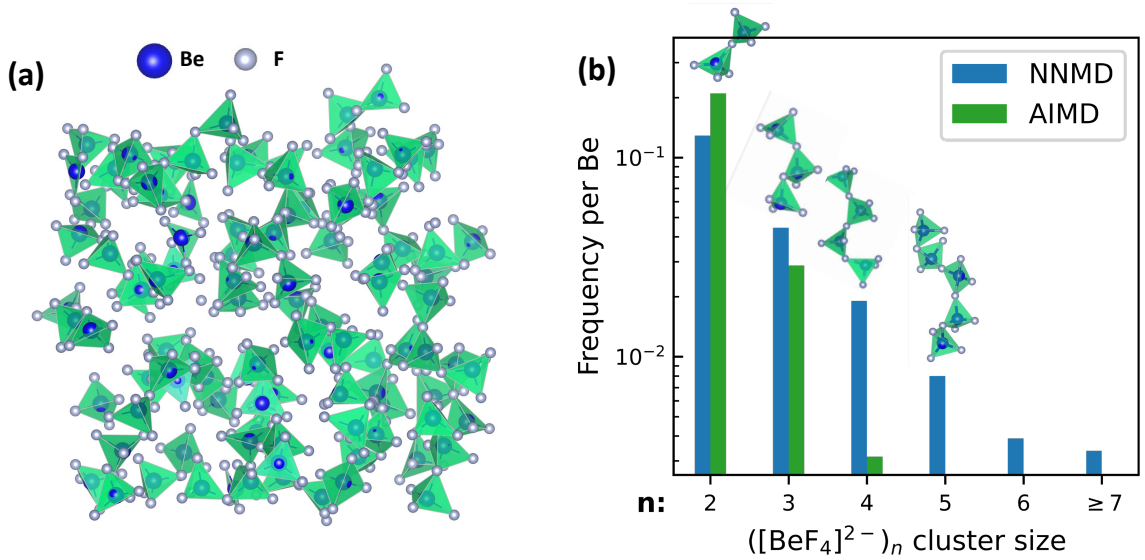

Fig. 6 (a) Snapshots of $([BeF_4]^{2-})_n$ clusters from FLiBe NNMD simulations at 700 °C with Li atoms removed from the visualization in VESTA[87]. Note, the F atoms were made smaller than Be for clarity. (b) The $([BeF_4]^{2-})_n$ cluster size distribution normalized by the number of Be atoms comparing AIMD and NNMD results. The snapshots of clusters with 2, 3, 4, and 5 Be cation centers are shown as a guide.

4 Discussion

The coordination numbers of Be by fluorine, as calculated from AIMD and NNMD simulations, are compared with the experimental values calculated from our neutron measurements in Table 1. We find that these results agree to the nearest integer value, with the experimental values showing a slightly lower CN. Our CN calculations agree with other experimentally and computationally determined values.[42,51,52,60]

As seen in Fig. 4d, AIMD is able to accurately predict $S(Q)$ for $Q > 4\,\text{Å}^{-1}$, corresponding to the local structure within the first solvation shell. We evaluate the agreement of the AIMD predicted structure factor with neutron measurements to be $R_\chi = 7.7\%$ for the neutron $S^n(Q)$. However, AIMD-simulated spectra show significant differences in the peak heights and distances for $Q < 4\,\text{Å}^{-1}$, showing inaccurate predictions of bond lengths and coordinations of intermediate range structures. This is due to the small cell limitations of AIMD simulations, in which intermediate structures interact with their self-images across periodic boundary conditions. These limitations cause AIMD simulations to produce an artificial cutoff on the intermediate range structure, which are better represented in NNMD simulations due to larger cell sizes.

A better insight into this can be obtained by quantitatively comparing the $([BeF_4]^{2-})_n$ cluster sizes between AIMD and NNMD simulations. To identify the $([BeF_4]^{2-})_n$ clusters in the melt, the F−Be bond length was chosen to be 2.35 Å which was obtained from the r_{min} value found in the F−Be partial PDF. The number of clusters of each size n were counted throughout the equilibrated NNMD and AIMD trajectories and were then normalized by the total number of Be atoms in each system. The distribution of cluster sizes larger than 2 is shown in Fig. 6b. It was found that the occurrence of large $([BeF_4]^{2-})_n$ clusters (with $n \geq 4$) are less prominent in AIMD simulations compared to NNMD, resulting in a greater mismatch in $S(Q)$ for $Q < 4\,\text{Å}^{-1}$ in Figs. 4d and 5d. Meanwhile, as beryllium fluoride intermediate-range structures are better represented in large cell NNMD simulations, the NNMD predicted $S(Q)$ features (peak heights and positions) agree very well down to the lowest Q values with minor mismatches with a $R_\chi = 2.7\%$ for the neutron $S^n(Q)$. The first peak at $1.7\,\text{Å}^{-1}$ corresponds to the Be−F correlations in $([BeF_4]^{2-})_n$ clusters present in the melt at 700 °C, which illustrates the presence of ordering effects in $2\text{LiF}-\text{BeF}_2$. An increase in ordering beyond the first shell (e.g., Be−Be), would cause a commensurate increase in the peak height as shown in Figs. 4d and 5d. As such, our NNMD simulations with large cell size of ∼21 Å and simulation time of nearly 1.5 ns (compared to ∼10.33 Å and 0.05 ns for AIMD) were sufficient for accurately sampling intermediate range structures. These simulation conditions (size, timescale) were chosen to ensure convergence of the structure distribution of linked $([BeF_4]^{2-})_n$ clusters, as shown in Fig. 6 for FLiBe at 700 °C, which is achieved with efficient ML-based simulations. Here, the disagreement between experiment and simulation could be caused by errors in predicting long-range interactions at the level of DFT and the interatomic potential fitting.

A further insight of FLiBe structure as predicted in AIMD and NNMD simulations can be gained by bond angle distribution analysis as shown in Fig. 7. Both AIMD and NNMD predict average F−Be−F angle ∼108° which corresponds to tetrahedral beryllium fluoride (Fig. 7a). The peak in Be−F−Be angle distribution (Fig. 7b) corresponds to corner-sharing beryllium fluoride complexes which lead to extended-range ordering in the melt. Both F−Be−F and Be−F−Be angle distribution plots are normalized such that their area integrates to one.

The demonstrated ability of NNIP to accurately predict intermediate-range structures and their populations despite being trained on small DFT simulation cells can be attributed to 1) training on a diverse range of configurations beyond a single AIMD trajectory and 2) sufficient charge-screening of long-

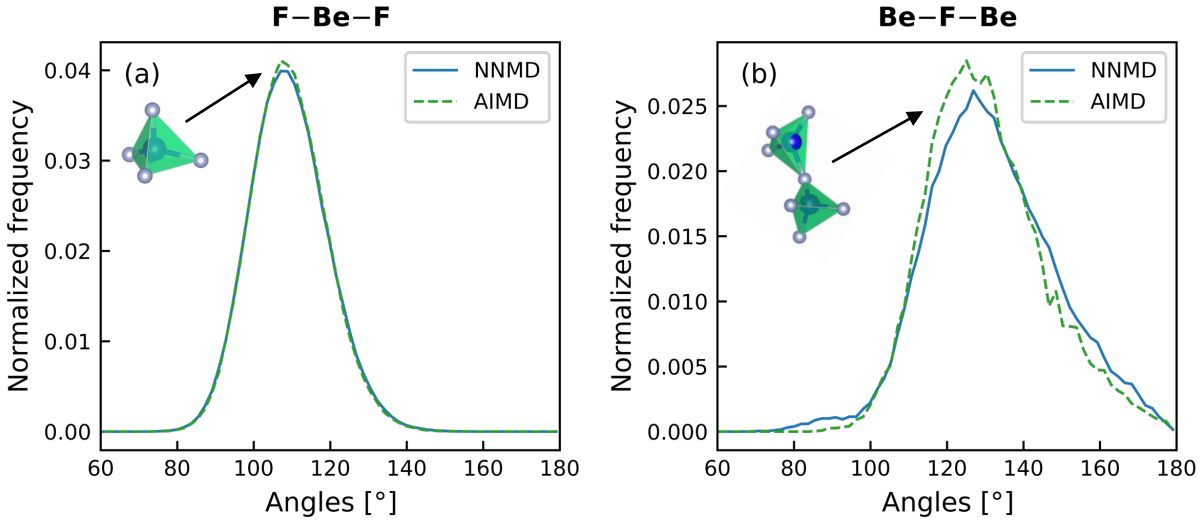

Fig. 7 The (a) F−Be−F and (b) Be−F−Be bond angle distribution from molecular dynamics simulations normalized such that they integrate to one.

range interactions in FLiBe. First, training the NNIP on configurations sampled at both 510 °C and 700 °C enables accurate interpolation of atomic forces and energies over the wide range NNMD-predicted configurations. Second, it is believed that the electrostatic potential beyond the 8 Å NNIP cutoff are sufficiently screened by polarizable solvent ions. This is consistent with our previous studies of other molten salts containing multivalent cations,[53] in which NNMD-predicted structures were supported by Raman spectroscopy. However, we note from our previous investigation[89] that it is possible for compounding approximations of semi-empirical DFT-VdW functionals and the NNIP truncation beyond 8 Å to induce larger errors for those systems and properties that are more strongly influenced by long-range interactions. In such cases, other considerations may be required for the explicit treatment of these effects. Here, the NNIP agrees with the scattering structure factor, providing confidence in the structural analysis.

5 Conclusions

In conclusion, we have performed neutron and X-ray total scattering measurements along with AIMD and NNMD simulations to characterize the molten structure of FLiBe. Our total scattering experiments match previous measurements both in the structure factor and the calculation of the coordination numbers. Both the AIMD and NNMD simulations captured the structure factor for $Q > 5\,\text{Å}^{-1}$, while the significant improvements in speed of NNMD simulations enabled larger box sizes that capture the intermediate range structure seen for $Q < 5\,\text{Å}^{-1}$. The combination of neutron and X-ray scattering experiments with NNMD simulations confirms the existence of intermediate range order comprised of corner-sharing tetrahedral $([BeF_4]^{2-})_n$ oligomers. The consistency among experimental and computational studies at higher resolution and computational efficiency than before give confidence that this structural characterization may serve as a reference for future investigations of fluoroberyllate melt structure and properties.

Data availability

The experimental and computational data on the molten structure of FLiBe will be available upon publication.

Conflicts of interest

At the time at which the article is published, some of the authors of this manuscript have interests in or relationships with entities that are commercializing nuclear technology. The content of this manuscript or the direction of the research presented herein was not influenced by these entities, nor by the authors' relationships with these entities.

Author contributions

D.N.G., H.W., J.M., R.C.G designed and prepared neutron samples. G.Z., D.S., B.K. designed and prepared X-ray samples. S.F., D.N.G., J.C.N. collected neutron measurements. D.S., D.O. collected X-ray measurements. S.F., J.C.N. analyzed neutron measurements. S.F., D.S., J.C.N, D.O. analyzed X-ray measurements. R.C., S.L. developed, conducted, and analyzed results from simulations. J.M., R.C.G., M.A., S.L., R.O.S., B.K. conceptualized the project. S.L, R.O.S, B.K. acquired funding. S.F., R.C., H.W., S.L, B.K. wrote and edited the manuscript. All authors discussed the results and reviewed the manuscript.

Acknowledgements

This material is based upon work supported by the U.S. Department of Energy, Office of Nuclear Energy, under Award Number 21-24563 (sample preparations, neutron, and X-ray measurements). The authors also acknowledge funding from the Los Alamos National Laboratory under subcontract 22206, through LANL Laboratory Directed Research and Development (LDRD) Project #20210113DR (neutron diffraction data analysis), and DOE-NE's Nuclear Energy University Program (NEUP) under

Award DE-NE0009204. A portion of this research used resources of the National Energy Research Scientific Computing Center, a DOE Office of Science User Facility supported by the Office of Science of the U.S. Department of Energy under Contract No. DE-AC02-05CH11231 using NERSC award BES-ERCAP0022445. A portion of this research used the 28-ID-1 beamline of the National Synchrotron Light Source II, a U.S. Department of Energy (DOE) Office of Science User Facility operated for the DOE Office of Science by Brookhaven National Laboratory under Contract No. DE-SC0012704. A portion of this research used resources at the Spallation Neutron Source, a DOE Office of Science User Facility operated by the Oak Ridge National Laboratory.

Notes and references

1 D. F. Williams and P. F. Britt, *Technology and Applied R&D Needs for Molten Salt Chemistry*, Oak Ridge National Laboratory (ORNL) technical Report, 2017.

2 P. N. Haubenreich and J. R. Engel, *Nuclear Applications and Technology*, 1970, **8**, 118–136.

3 H. G. MacPherson, *Nuclear Science and Engineering*, 1985, **90**, 374–380.

4 L. Mathieu, D. Heuer, R. Brissot, C. Garzenne, C. Le Brun, D. Lecarpentier, E. Liatard, J. M. Loiseaux, O. Méplan, E. Merle-Lucotte, A. Nuttin, E. Walle and J. Wilson, *Progress in Nuclear Energy*, 2006, **48**, 664–679.

5 V. V. Ignatiev, O. S. Feynberg, A. V. Zagnitko, A. V. Merzlyakov, A. I. Surenkov, A. V. Panov, V. G. Subbotin, V. K. Afonichkin, V. A. Khokhlov and M. V. Kormilitsyn, *Atomic Energy*, 2012, **112**, 157–165.

6 C. Andreades, A. T. Cisneros, J. K. Choi, A. Y. K. Chong, M. Fratoni, S. Hong, L. R. Huddar, K. D. Huff, J. Kendrick, D. L. Krumwiede, M. R. Laufer, M. Munk, R. O. Scarlat and N. Zweibau, *Nuclear Technology*, 2016, **195**, 223–238.

7 B. N. Sorbom, J. Ball, T. R. Palmer, F. J. Mangiarotti, J. M. Sierchio, P. Bonoli, C. Kasten, D. A. Sutherland, H. S. Barnard, C. B. Haakonsen, J. Goh, C. Sung and D. G. Whyte, *Fusion Engineering and Design*, 2015, **100**, 378–405.

8 C. Forsberg, G. Zheng, R. G. Ballinger and S. T. Lam, *Nuclear Technology*, 2020, **206**, 1778–1801.

9 C. W. Forsberg, *Nuclear Technology*, 2020, **206**, 1659–1685.

10 B. Mignacca and G. Locatelli, *Progress in Nuclear Energy*, 2020, **129**, 103503.

11 R. W. Moir, *Energy Conversion and Management*, 2008, **49**, 1849–1858.

12 B. M. Elsheikh, *Journal of Radiation Research and Applied Sciences*, 2013, **6**, 63–70.

13 D. F. Williams and K. T. Clarno, *Nuclear Technology*, 2008, **163**, 330–343.

14 V. Khokhlov, V. Ignatiev and V. Afonichkin, *Journal of Fluorine Chemistry*, 2009, **130**, 30–37.

15 Sylvie. Delpech, C. Cabet, C. Slim and G. S. Picard, *Materials Today*, 2010, **13**, 34–41.

16 W. R. Grimes, *Nuclear Applications and Technology*, 1970, **8**, 137–155.

17 M. S. Sohal, M. A. Ebner, P. Sabharwall and P. Sharpe, *Engineering Database of Liquid Salt Thermophysical and Thermochemical Properties*, Idaho National Lab. (INL), Idaho Falls, ID (United States) Technical Report INL/EXT-10-18297, 2010.

18 S. Cantor, W. T. Ward and C. T. Moynihan, *The Journal of Chemical Physics*, 1969, **50**, 2874–2879.

19 O. Yu. Tkacheva, A. V. Rudenko, A. A. Kataev, P. N. Mushnikov, A. S. Kholkina and Yu. P. Zaikov, *Russian Journal of Non-Ferrous Metals*, 2022, **63**, 276–283.

20 K. Yajima, H. Moriyama, J. Oishi and Y. Tominaga, *The Journal of Physical Chemistry*, 1982, **86**, 4193–4196.

21 T. Lichtenstein, M. A. Rose, J. Krueger, E. Wu and M. A. Williamson, 2020, 34.

22 E. Il'ina, P. Mushnikov, S. Pershina, A. Rudenko, A. Redkin, Yu. Zaikov, A. Kholkina and V. Voronin, *Journal of Molecular Liquids*, 2021, **344**, 117731.

23 R. Vidrio, S. Mastromarino, E. Still, L. Chapdelaine and R. O. Scarlat, *Journal of Chemical & Engineering Data*, 2022.

24 D. R. Olander, G. T. Fukuda and C. F. Baes, *Fusion Science and Technology*, 2002, **41**, 141–150.

25 M. R. Zaghloul, D. K. Sze and A. R. Raffray, *Fusion Science and Technology*, 2003, **44**, 344–350.

26 S. Fukada and A. Nakamura, *Fusion Science and Technology*, 2014, **66**, 322–336.

27 B. F. Hitch and C. F. J. Baes, *Inorganic Chemistry*, 1969, **8**, 201–207.

28 K. A. Romberger, J. Braustein and R. E. Thoma, *The Journal of Physical Chemistry*, 1972, **76**, 1154–1159.

29 K. Igarashi, Y. Okamoto, J. Mochinaga and H. Ohno, *Journal of the Chemical Society, Faraday Transactions 1: Physical Chemistry in Condensed Phases*, 1988, **84**, 4407–4415.

30 B. A. Frandsen, S. D. Nickerson, A. D. Clark, A. Solano, R. Baral, J. Williams, J. Neuefeind and M. Memmott, *Journal of Nuclear Materials*, 2020, **537**, 152219.

31 Q.-J. Li, D. Sprouster, G. Zheng, J. C. Neuefeind, A. D. Braatz, J. Mcfarlane, D. Olds, S. Lam, J. Li and B. Khaykovich, *ACS Applied Energy Materials*, 2021, **4**, 3044–3056.

32 D. Sprouster, G. Zheng, S.-C. Lee, D. Olds, C. Agca, J. McFarlane, Y. Z and B. Khaykovich, *ACS Applied Energy Materials*, 2022.

33 M. Kondo, T. Nagasaka, A. Sagara, N. Noda, T. Muroga, Q. Xu, M. Nagura, A. Suzuki and T. Terai, *Journal of Nuclear Materials*, 2009, **386–388**, 685–688.

34 L. C. Olson, J. W. Ambrosek, K. Sridharan, M. H. Anderson and T. R. Allen, *Journal of Fluorine Chemistry*, 2009, **130**, 67–73.

35 G. Zheng, B. Kelleher, G. Cao, M. Anderson, T. Allen and K. Sridharan, *Journal of Nuclear Materials*, 2015, **461**, 143–150.

36 S. Guo, J. Zhang, W. Wu and W. Zhou, *Progress in Materials Science*, 2018, **97**, 448–487.

37 J. Zhang, C. W. Forsberg, M. F. Simpson, S. Guo, S. T. Lam, R. O. Scarlat, F. Carotti, K. J. Chan, P. M. Singh, W. Doniger, K. Sridharan and J. R. Keiser, *Corrosion Science*, 2018, **144**, 44–53.

38 S. Fayfar, G. Zheng, D. Sprouster, M. S. J. Marshall, E. Stavitski, D. Leshchev and B. Khaykovich, *ACS Omega*, 2023, **8**, 24673–24679.

39 M. Salanne, C. Simon, P. Turq, R. J. Heaton and P. A. Madden, *Journal of Physical Chemistry B*, 2006, **110**, 11461–11467.

40 T. Porter, M. M. Vaka, P. Steenblik and D. Della Corte, *Communications Chemistry*, 2022, **5**, 1–15.

41 A. L. Smith, E. Capelli, R. J. M. Konings and A. E. Gheribi, *Journal of Molecular Liquids*, 2020, **299**, 112165.

42 F. Vaslow and A. H. Narten, *The Journal of Chemical Physics*, 1973, **59**, 4955–4960.

43 C. F. Baes, *Journal of Solid State Chemistry*, 1970, **1**, 159–169.

44 A. Rahman, R. H. Fowler and A. H. Narten, *The Journal of Chemical Physics*, 1972, **57**, 3010–3011.

45 G. E. Moore, *Chemistry Division Annual Progress Report for Period Ending May 20, 1974*, Oak Ridge National Lab., Tenn. (USA) Technical Report ORNL-4706, 1974.

46 A. S. Quist, J. B. Bates and G. E. Boyd, *The Journal of Physical Chemistry*, 1972, **76**, 78–83.

47 L. M. Toth, J. B. Bates and G. E. Boyd, *The Journal of Physical Chemistry*, 1973, **77**, 216–221.

48 J. Dai, H. Han, Q. Li and P. Huai, *Journal of Molecular Liquids*, 2016, **213**, 17–22.

49 Y. Li, X. Liu, B. Wang and C. Wang, *Journal of Molecular Liquids*, 2021, **325**, 115208.

50 K. Baral, S. San, R. Sakidja, A. Couet, K. Sridharan and W.-Y. Ching, *ACS Omega*, 2021, **6**, 19822–19835.

51 S. Attarian, D. Morgan and I. Szlufarska, *Journal of Molecular Liquids*, 2022, **368**, 120803.

52 N. Winner, H. Williams, R. O. Scarlat and M. Asta, *Journal of Molecular Liquids*, 2021, **335**, 116351.

53 R. Chahal, S. Roy, M. Brehm, S. Banerjee, V. Bryantsev and S. T. Lam, *JACS Au*, 2022, **2**, 2693–2702.

54 J. Behler and M. Parrinello, *Physical Review Letters*, 2007, **98**, 146401.

55 L. Zhang, J. Han, H. Wang, R. Car and W. E, *Physical Review Letters*, 2018, **120**, 143001.

56 A. Rodriguez, S. Lam and M. Hu, 2021.

57 S. T. Lam, Q.-J. Li, R. Ballinger, C. Forsberg and J. Li, *ACS Applied Materials & Interfaces*, 2021, **13**, 24582–24592.

58 S.-C. Lee, Y. Zhai, Z. Li, N. P. Walter, M. Rose, B. J. Heuser and Y. Z, *The Journal of Physical Chemistry B*, 2021, **125**, 10562–10570.

59 S. Lam, Q.-J. Li, J. Mailoa, C. Forsberg, R. Ballinger and J. Li, *Journal of Materials Chemistry A*, 2021, **9**, 1784–1794.

60 H. Wang, B. Yue, L. Yan, T. Jiang and S. Peng, *Journal of Molecular Liquids*, 2022, **345**, 117027.

61 G. J. Janz, G. L. Gardner, U. Krebs and R. P. T. Tomkins, *Journal of Physical and Chemical Reference Data*, 2009, **3**, 1–115.

62 L. Martínez, R. Andrade, E. G. Birgin and J. M. Martínez, *Journal of Computational Chemistry*, 2009, **30**, 2157–2164.

63 R. Chahal, S. Banerjee and S. T. Lam, *Frontiers in Physics*, 2022, **10**, year.

64 H. Wang, L. Zhang, J. Han and W. E, *Computer Physics Communications*, 2018, **228**, 178–184.

65 L. Zhang, J. Han, H. Wang, W. Saidi, R. Car and W. E, Advances in Neural Information Processing Systems, 2018.

66 S. Plimpton, *Journal of Computational Physics*, 1995, **117**, 1–19.

67 W. G. Hoover, *Physical Review A*, 1985, **31**, 1695–1697.

68 J. Neuefeind, M. Feygenson, J. Carruth, R. Hoffmann and K. K. Chipley, *Nuclear Instruments and Methods in Physics Research Section B: Beam Interactions with Materials and Atoms*, 2012, **287**, 68–75.

69 M. T. McDonnell, D. P. Olds, K. L. Page, J. C. Neufeind, M. G. Tucker, J. C. Bilheux, W. Zhou and P. F. Peterson, *Acta Crystallographica Section A Foundations and Advances*, 2017, **73**, a377–a377.

70 O. Ivashkevych, M. Abeykoon, J. Adams, G. Bischof, E. Dooryhee, J. Li, R. Petkus, J. Trunk and Z. Yin, 17th International Conference on Accelerator and Large Experimental Physics Control Systems (ICALEPCS'19), New York, NY, USA, 05-11 October 2019, 2020, pp. 1584–1589.

71 J. Kieffer and D. Karkoulis, *Journal of Physics: Conference Series*, 2013, **425**, 202012.

72 P. Juhás, T. Davis, C. L. Farrow and S. J. L. Billinge, *Journal of Applied Crystallography*, 2013, **46**, 560–566.

73 P. J. Brown, A. G. Fox, E. N. Maslen, M. A. O'Keefe and B. T. M. Willis, *International Tables for Crystallography*, International Union of Crystallography, Chester, England, 1st edn, 2006, vol. C, pp. 554–595.

74 J. Neuefeind, *Journal of Molecular Liquids*, 2002, **98–99**, 87–95.

75 H. E. Fischer, A. C. Barnes and P. S. Salmon, *Reports on Progress in Physics*, 2006, **69**, 233–299.

76 P. F. Peterson, D. Olds, M. T. McDonnell and K. Page, *Journal of Applied Crystallography*, 2021, **54**, 317–332.

77 K. Zhou and B. Liu, *Molecular Dynamics Simulation: Fundamentals and Applications*, Elsevier, Amsterdam Kidlington Cambridge, Mass, 2022.

78 A. K. Soper, *GudrunN and GudrunX: Programs for Correcting Raw Neutron and X-ray Diffraction Data to Differential Scattering Cross Section*, Science & Technology Facilities Council Swindon, UK, 2011.

79 P. B. Lond, P. S. Salmon and D. C. Champeney, *Journal of the American Chemical Society*, 1991, **113**, 6420–6425.

80 A. C. Hannon and J. M. Parker, *Journal of Non-Crystalline Solids*, 2000, **274**, 102–109.

81 L. Hennet, J. W. E. Drewitt, D. R. Neuville, V. Cristiglio, J. Kozaily, S. Brassamin, D. Zanghi and H. E. Fischer, *Journal of Non-Crystalline Solids*, 2016, **451**, 89–93.

82 A. C. Wright, *Journal of Non-Crystalline Solids*, 1994, **179**, 84–115.

83 J. Du, C. J. Benmore, R. Corrales, R. T. Hart and J. K. R. Weber, *Journal of Physics: Condensed Matter*, 2009, **21**, 205102.

84 O. L. G. Alderman, G. Ferlat, A. Baroni, M. Salanne, M. Micoulaut, C. J. Benmore, A. Lin, A. Tamalonis and J. K. R. Weber, *Journal of Physics: Condensed Matter*, 2015, **27**, 455104.

85 M. Wilson, *Journal of Physics: Condensed Matter*, 2016, **28**, 503001.
86 Q. Zhou, Y. Shi, B. Deng, J. Neuefeind and M. Bauchy, *Science Advances*, 2021, **7**, eabh1761.
87 K. Momma and F. Izumi, *Journal of Applied Crystallography*, 2011, **44**, 1272–1276.
88 S. Sharma, A. S. Ivanov and C. J. Margulis, *The Journal of Physical Chemistry B*, 2021, **125**, 6359–6372.
89 S. Lam, S. Banerjee and R. Chahal, Transactions of the American Nuclear Society, 2022, pp. 385–386.